journal of the mechanical behavior of biomedical materials 126 (2022) 104952

Contents lists available at ScienceDirect

Journal of the Mechanical Behavior of Biomedical Materials

journal homepage: www.elsevier.com/locate/jmbbm

Research paper

Cortex tissue relaxation and slow to medium load rates dependency can be captured by a two-phase flow poroelastic model

Stéphane Urcun [a,b,c], Pierre-Yves Rohan [b], Giuseppe Sciumè [c], Stéphane P.A. Bordas [a,*]

[a] Institute for Computational Engineering Sciences, Department of Engineering Sciences, Faculté des Sciences, de la Technologie et de Médecine, Université du Luxembourg, Campus Kirchberg, Luxembourg
[b] Institut de Biomécanique Humaine Georges Charpak, Arts et Métiers ParisTech, Paris, France
[c] Institut de Mécanique et d'Ingénierie (I2M), Univ. Bordeaux, CNRS, ENSAM, Bordeaux INP, Talence, France

ARTICLE INFO

Keywords:
Poromechanics
Brain tissue
Mechanical testing

ABSTRACT

This paper investigates the complex time-dependent behavior of cortex tissue, under adiabatic condition, using a two-phase flow poroelastic model. Motivated by experiments and Biot's consolidation theory, we tackle time-dependent uniaxial loading, confined and unconfined, with various geometries and loading rates from 1 μm/s to 100 μm/s. The cortex tissue is modeled as the porous solid saturated by two immiscible fluids, with dynamic viscosities separated by four orders, resulting in two different characteristic times. These are respectively associated to interstitial fluid and glial cells. The partial differential equations system is discretized in space by the finite element method and in time by Euler-implicit scheme. The solution is computed using a monolithic scheme within the open-source computational framework FEniCS. The parameters calibration is based on Sobol sensitivity analysis, which divides them into two groups: the tissue specific group, whose parameters represent general properties, and sample specific group, whose parameters have greater variations. Our results show that the experimental curves can be reproduced without the need to resort to viscous solid effects, by adding an additional fluid phase. Through this process, we aim to present multiphase poromechanics as a promising way to a unified brain tissue modeling framework in a variety of settings.

1. Introduction

The biomechanical characterization of human brain tissue and the development of appropriate mechanical models is crucial to provide realistic computational predictions. These predictions can assist in understanding the mechanical environment involved in neurodevelopment and neurological disorders (Budday et al., 2014a; Seo et al., 2016), in simulating traumatic brain injury, to investigate the mechanical pathogenesis of head trauma (Basilio et al., 2019) and in studying head injuries and developing protection systems (Forero Rueda et al., 2011). Mathematical modeling is also the key to devising brain surgery simulation for training, assistance and guidance (Bui et al., 2018a,b).

From an experimental perspective, several sophisticated mechanical tests have been proposed and conducted both on human and animal brain tissue in the past decades (see Budday et al., 2019 for a complete review). These have consistently shown that brain tissue is non-linear, asymmetric in tension–compression and sensitive to loading rates. Moreover, gray and white matter, when they are isolated, exhibit different stiffness and brain tissue can be separated into four regions, with their own mechanical profile: cortex, corona radiata, basal ganglia and corpus callosum. It has been shown that the mechanical response of brain tissue is sensitive to the time scale and the characteristic length of loading. This has been attributed by several authors to the ultra-soft, gel-like nature of brain tissue, which implies that effects on very small length and time scales may hold an important impact on the overall mechanical behavior (Budday et al., 2019).

To capture the mechanical response of brain tissue, several constitutive models have been proposed based on the type and range of the strain rates associated with pathological and normal conditions. In particular, extensive research has been conducted for brain matter experiencing compression at quasi-static loading (Rashid et al., 2012; Chatelin et al., 2010). These studies have shaped our understanding of the hyperelastic time-independent response of human brain tissue. However, its time-dependent behavior at finite strains and under various loading conditions remains insufficiently understood.

Visco-elastic models (MacManus et al., 2017; Budday et al., 2017, 2018; Ning et al., 2006) are typically chosen to reproduce the time-dependent, hysteresis, preconditioning softening (regarding this topic, see the review Budday et al., 2019 section 3.5) as well as the stress

* Corresponding author.
E-mail address: stephane.bordas@alum.northwestern.edu (S.P.A. Bordas).

https://doi.org/10.1016/j.jmbbm.2021.104952
Received 25 July 2021; Received in revised form 16 October 2021; Accepted 27 October 2021
Available online 30 November 2021
1751-6161/

relaxation observed in experiments. The coupling of large deformation (usually hyper-elastic) and visco-elasticity has allowed to accurately capture various deformation types in a large range of strain. These have been employed to predict the essential features of brain tissue: non-linearity, hysteresis, and tension–compression asymmetry. Yet, most models developed to date have been tailored to reproduce particular loading scenarios or for specific applications. We conclude that this specific kind of models, that could be denoted as phenomenological, do not contain the required components to be transferable from one type of experimental conditions to another. Our aim is to alleviate these deficiencies, so that models developed for one patient can be used for another patient, and to make this possible for the most varied types of boundary and environmental conditions. We propose in this paper a particular multi-phase poro-elastic model. We show that this model, once calibrated on a certain set of experiments, can also reproduce the behavior of brain tissue observed in completely different loading conditions. We therefore hypothesize that such a model could be a sound starting point for a generic mechanical model of the brain. In the appendix, the interested reader may also find the indication that, for a viscoelastic model, to mimic the behavior of a porous material, the parameters must be adjusted according to the specimen size.

Several studies (Franceschini et al., 2006; Cheng and Bilston, 2007; Haslach et al., 2014), based on a series of consolidation tests, suggested that extracellular fluid flow dominates the apparent viscoelastic properties of brain tissue. Based on mixture theory, poroelasticity has been extensively used to model brain tissue (Lefever et al., 2013; Lang et al., 2014; Ehlers and Wagner, 2015a; Fletcher et al., 2014; Dutta-Roy et al., 2008). Porous media mechanics, (Biot, 1941), which describe the mechanical behavior of a porous solid containing viscous fluid, are compatible with processes which involve low-strain-rate deformations of the brain, such as edema, hydrocephalus, hemorrhage (Nagashima et al., 1987; Owler et al., 2004) and infusion (Sobey et al., 2012; Li et al., 2013). However, single phase flow poromechanics show limitation to render the highly non-linear behavior of the brain tissue. Franceschini et al. (2006) conclude that consolidation (deformation of the solid matrix due to pore fluid flow and its drainage from the interstitial space) is the leading mechanism in quasi-static deformation of brain tissue. To achieve complete adherence between their experimental data and their theoretical formulations, they conclude that the addition of a viscous component to the rheological model is necessary.

This last point remains a matter of debate. Budday et al. (2019) hypothesized that brain tissue rheology is characterized by at least two different timescales, which are attributed to viscous and porous effects, respectively. The viscous response can be related to the intracellular interactions within the network of cells forming the solid phase of the tissue, while the porous medium behavior is associated with the interaction between the solid and fluid phase. In a recent study, Comellas et al. (2020) explored in details the interplay between single phase poro-elasticity and finite visco-elasticity. Their model is capable of accurately reproducing consolidation, shear stress and cycle loading tests. However, the respective influence of porous and viscous components are strongly dependent on the parameters calibration, which could impede the physical interpretation of the results.

Unlike conventional approaches that combine viscoelastic and poroelastic behaviors into a single framework (Hosseini-Farid et al., 2020), we hypothesize in this article that a two-phase flow poroelasticity can also capture the stress relaxation and the sensitivity of a set of selected load rates. The two fluid phases, with their respective dynamic viscosities, allow for reproducing the two different time scales. As a first step, we limited our study on the cortex region of the brain, which is known to be soft and isotropic (Budday et al., 2019). We first reproduce the experimental results of Franceschini et al. (2006) without the use of a viscoelastic solid and, with the same model, we reproduce the experimental set of Budday et al. (2015) composed of various indenters, load rates and stress relaxation.

Table 1
Characteristics of the indentation tests on *ex vivo* bovine cortex (Budday et al., 2015). Test 1, 2 and 3 belong to long range indentation tests, Test 4 is a relaxation test.

Characteristics	Test 1	Test 2	Test 3	Test 4
Indentation depth μm	300	300	300	100
Load rate μm/s	5	5	1	100
Indenter ⌀ mm	1	0.75	0.75	1.5
Unloading of 300 μm	Yes	Yes	Yes	No
Holding of 600 s	No	No	No	Yes

2. Experimental data

Consolidation tests

The consolidation test (an uniaxial strain under free drainage conditions) is crucial for poromechanical modeling, as this strain cannot be reproduced by an elastic law and is not adapted to viscoelastic models (Franceschini et al., 2006). In this contribution we chose to reproduce the experiment of Franceschini conducted on N = 12 specimens. The experimental procedure is briefly reported here. For more details the interested reader could refer to Franceschini et al. (2006).

Twelve human parietal lobe cylindrical samples of 30 mm diameter and 5 to 8 mm height are harvested, within 12 h after death, and placed into a consolidometer specifically designed for the tests, shown in Fig. 1A. The top and bottom of the samples are under free drainage conditions, using a filter paper against a porous brass employed in geotechnical consolidometer.

We identify three different profiles on the twelve samples, where the same initial load (6 Newton) will lead deformation from 3.5% to 6.5%. We retrieve the same three profiles on the 3 Newton load series. As a consequence, we select six samples from Franceschini et al. (2006) for this study, one of each profile for the 3 and 6 Newton one step loads. We adopt the following nomenclature for the samples: XN for X Newton load series, followed by the figure index and letter of Franceschini et al. (2006), *e.g.* 3N C2 a.

Indentation tests

Due to the difficulties in producing consistent samples, and due to the alterations to the micro-structural arrangement during the sample preparation, it has been reported that stiffness values using confined compression creep and stress relaxation tests are often not reproducible and may vary by an order of magnitude or more. Indentation has been shown to provide a robust, reliable, and repeatable method to quantify the mechanical properties in situ without altering the local micro-architectural arrangement.

Four indentation tests on *ex vivo* bovine gray matter, within 6 h after death, are reproduced. These are subsets of the long range indentation type, on $N = 192$ samples, described in Budday et al. (2015). Before any test, all samples are subjected to a 100 μm indentation depth to stabilize the material response and ensure parallelism. The experimental design is shown in Fig. 2A and the characteristics of the tests can be found in Table 1. Budday et al. present indentation tests with loading rates between 1 μm/s and 100 μm/s, for reason of brevity, we choose to reproduce these extreme values without the intermediate 10 μm/s and 20 μm/s. In Budday et al. (2015), Budday et al. present mean experimental curves for each test and indicate 21% of standard deviation in the set of samples.

3. Mathematical modeling

The descriptions of cortex tissue as a porous medium can take several forms: a solid scaffold saturated by a fluid (Hakim et al., 1976), a visco-elastic scaffold saturated by a fluid (Franceschini et al., 2006), an elastic scaffold separated into two compartments, vascular and extra-vascular, each saturated by a different fluid (Ehlers and Wagner, 2015b), among others. In this study, we focus on *ex vivo* material, so

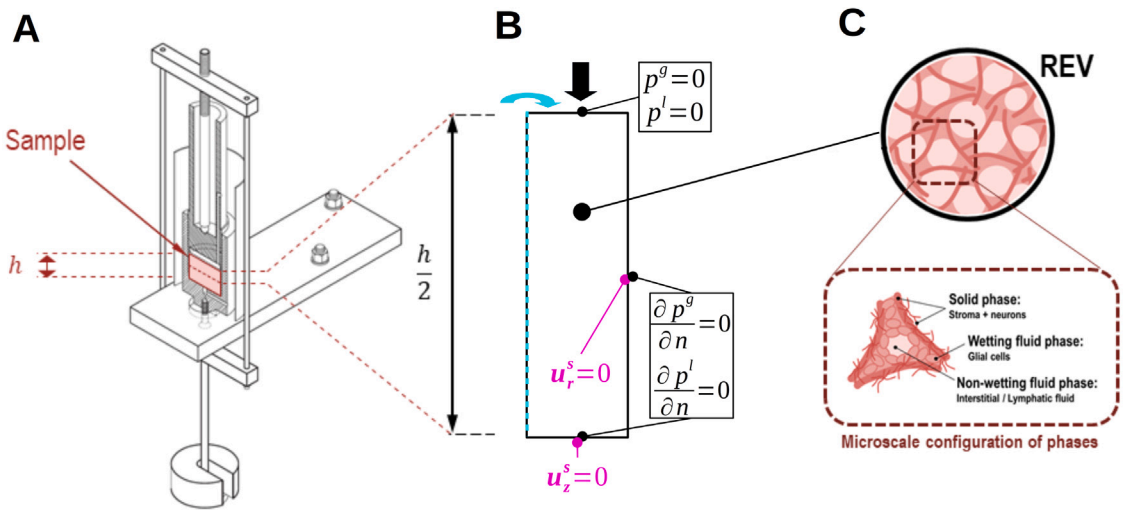

Fig. 1. Consolidation tests on *ex vivo* human cortex (Franceschini et al., 2006). **A** Experimental design of consolidometer of Franceschini et al. (2006). **B** Boundary conditions of the physical problem: the fluids are free to escape to loaded boundary (drained condition), the other boundaries are impervious; except at the loaded boundary, the displacement of the solid scaffold is allowed only on the tangential direction (slip condition). **C** Representative elementary volume (REV) with the phase components of the model framework. *Source:* **A** Reproduced with the authorization of the authors.

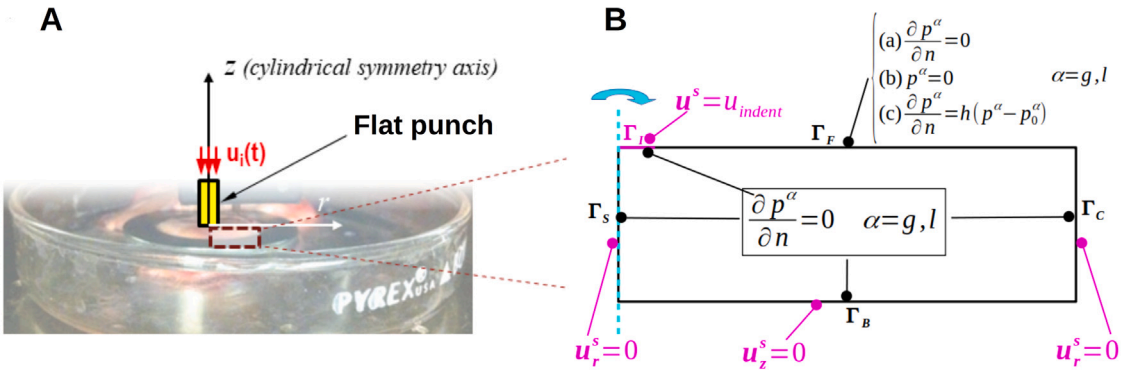

Fig. 2. Indentation test on *ex vivo* bovine cortex (Budday et al., 2015). **A** Experimental design of indentation tests of Budday et al. (2015). **B** The sample is considered under cylindrical symmetry hypothesis, $\mathbf{u}_i(t)$ is displacement prescribed by the indenter on the sample surface.
Source: **A** Reproduced with the authorization of the authors.

the vascular activity will be neglected and the vascular network will be considered a part of the solid scaffold. Within the parenchyma, we distinguish two fluid phases: glial g phase, for which we prescribed a dynamic viscosity close to gel-like, and interstitial/lymphatic l phase, with a prescribed dynamic viscosity one order higher than water. A summary of the representative elementary volume is shown in Fig. 1C. This specific description of cortex tissue by two immiscible fluids within a porous solid has no experimental equivalent. Therefore, we present the quantitative information to set the initial guess of the parameters from several sources in the experimental literature.

Governing equations

A porous medium consists in a solid scaffold, that is to say all the material that act as structural solids in the porous medium. Its volume fraction is denoted ε^s. The porosity is the volume fraction saturated by the fluids, denoted ε, and

$$\varepsilon^s + \varepsilon = 1 \tag{1}$$

We distinguish, in this contribution, the glial phase g from the remaining fluid phase l. These two phases are assumed to be immiscible fluids with their respective saturation S^l and S^g and

$$S^l + S^g = 1 \tag{2}$$

The volume occupied by the liquid phase and by the glial phase are respectively denoted εS^l and εS^g.

The mass balance of the porous solid reads:

$$\frac{\mathrm{D}^s}{\mathrm{D}t}(\rho^s\varepsilon^s) + \rho^s\varepsilon^s\nabla\cdot\mathbf{v}^{\bar{s}} = 0 \tag{3}$$

- with $\frac{\mathrm{D}^s}{\mathrm{D}t}(\rho^s\varepsilon^s)$ the evolution of the solid scaffold mass
- and $\rho^s\varepsilon^s\nabla\cdot\mathbf{v}^{\bar{s}}$ its flux term.

The mass balance of the fluids phases reads:

$$\frac{\mathrm{D}^s}{\mathrm{D}t}(\rho^g\varepsilon S^g) + \nabla\cdot\left(\rho^g\varepsilon S^g\mathbf{v}^{\overline{gs}}\right) + \rho^g\varepsilon S^g\nabla\cdot\mathbf{v}^{\bar{s}} = 0 \tag{4}$$

$$\frac{\mathrm{D}^s}{\mathrm{D}t}\left(\rho^l\varepsilon S^l\right) + \nabla\cdot\left(\rho^l\varepsilon S^l\mathbf{v}^{\overline{ls}}\right) + \rho^l\varepsilon S^l\nabla\cdot\mathbf{v}^{\bar{s}} = 0 \tag{5}$$

- with $\frac{\mathrm{D}^s}{\mathrm{D}t}(\rho^\alpha\varepsilon S^\alpha)$ the evolution of the fluid phase α
- $\nabla\cdot\left(\rho^\alpha\varepsilon S^\alpha\mathbf{v}^{\overline{\alpha s}}\right)$ the flux term of the phase α where $\mathbf{v}^{\overline{\alpha s}}$ is the phase α velocity relatively to the solid: $\mathbf{v}^{\overline{\alpha s}} = \mathbf{v}^{\bar{\alpha}} - \mathbf{v}^{\bar{s}}$
- and $\rho^\alpha\varepsilon S^\alpha\nabla\cdot\mathbf{v}^{\bar{s}}$ the contribution of the solid deformation to the mass conservation of the phase $\alpha = l, g$

Constitutive relationships

The glial phase will be denoted as the wetting phase, that is to say, the phase that preferentially covers the solid scaffold. Therefore, it is the one that sustains the mechanical load before transmitting it to the non-wetting phase, namely the liquid phase. The pressure relationship with the phases saturation is justified by the simplified entropy inequality of the thermodynamically constrained averaging theory (TCAT) (Gray and Miller, 2014). At the microscale equilibrium, it is assumed that the evolution of the interface surface is negligible compared to the evolution of the fluid saturation, therefore the interfacial tension between the phases is directly linked to the pressure difference (see Sciumè et al., 2014b). This implies a pressure jump between the wetting phase g and the non-wetting phase l, whose saturation S^l depends on the pressure jump $p^{lg} = p^l - p^g$ (see Eq. (6)).

From Sciumè et al. (2014b), the expression of the liquid phase saturation, dependent on the difference of the phases pressure, is adapted from the heuristic formulation of van Genuchten (1980):

$$S^l = \frac{2}{\pi}\arctan\left(\frac{p^{lg}}{a}\right) \tag{6}$$

with the theoretical parameter a, which represents the intensity of the interplay between the solid scaffold and the non-wetting phase. Its range commonly taken is $[500; 800]$ (see Sciumè et al., 2014,a; Mascheroni et al., 2016; Santagiuliana et al., 2019).

The solid scaffold has its intrinsic permeability k^s_{int} and follows linear elasticity (Young modulus E, Poisson's ratio ν):

$$\bar{\bar{\sigma}}_{\text{eff}} = \lambda tr(\bar{\bar{\epsilon}})\mathbb{I} + 2\mu\bar{\bar{\epsilon}} \tag{7}$$

with $\mathbb{I}$ the identity tensor, $\bar{\bar{\epsilon}}(\mathbf{u}^s) = \frac{1}{2}(\nabla\mathbf{u}^s + (\nabla\mathbf{u}^s)^T)$ the linearized strain tensor, and the Lamé constants $\lambda = \frac{E\nu}{(1+\nu)(1-2\nu)}$ and $\mu = \frac{E}{2(1+\nu)}$.

The two fluid phases have their own relative permeabilities:

$$k^l_{\text{rel}} = (S^l)^{A_l} \qquad k^g_{\text{rel}} = (S^g)^{B_g} \tag{8}$$

with A_l and B_g to be calibrated.

The interaction between fluid phases and the solid scaffold are modeled by a generalized Darcy's flow, deduced from the linear momentum conservation of fluid phases:

$$-\frac{k^\alpha_{\text{rel}}k^s_{\text{int}}}{\mu^\alpha}\nabla p^\alpha = \varepsilon S^\alpha(\mathbf{v}^{\bar{\alpha}s}) \qquad \alpha = g, l \tag{9}$$

where k^s_{int} is the intrinsic permeability of the solid scaffold, μ^α, k^α_{rel} and p^α are respectively the dynamic viscosity, relative permeability and the pressure of each fluid phase $\alpha = l, g$.

Final system of governing equations

The physical system is governed by the mass conservation of each phase and by linear momentum conservation of the overall system. The primary unknowns of the model are the solid scaffold displacement $\mathbf{u}^s$, the glial phase pressure p^g and the liquid phase pressure difference p^{lg}.

Eqs. (3)–(5) are treated as follows:

- Eq. (3) is injected into Eqs. (4)–(5) thanks to the constraint Eq. (1)
- the difference of order between the mechanical constrains and the compressibility of the components allows us to neglect the variation of their density, therefore ρ^α is considered constant $\alpha = s, g, l$. We also assume that the component have the same density $\rho^s = \rho^g = \rho^l$
- the evolution of the glial volume fraction $\varepsilon\frac{D^s S^l}{Dt}$ is expressed with respect to the constraint Eq. (2). Its evolution depends on the interstitial fluid pressure $S^l(p^{lg})$, see the constitutive relationship Eq. (6)

We obtain the following system:

$$\begin{cases} -\varepsilon\frac{dS^l}{dp^{lg}}\frac{D^s p^{lg}}{Dt} - \nabla\cdot\left[\frac{k^g_{\text{rel}}k^s_{\text{int}}}{\mu^g}\nabla p^g\right] + S^g\nabla\cdot\mathbf{v}^s = 0 \\ \varepsilon\frac{dS^l}{dp^{lg}}\frac{D^s p^{lg}}{Dt} - \nabla\cdot\left[\frac{k^l_{\text{rel}}k^s_{\text{int}}}{\mu^l}\nabla(p^g + p^{lg})\right] + S^l\nabla\cdot\mathbf{v}^s = 0 \end{cases} \tag{10}$$

The governing equations are completed with the momentum balance of the system:

$$\nabla\cdot\sigma_T = \mathbf{0} \qquad \text{with} \qquad \sigma_T = \sigma_{\text{eff}} - \beta p^s \tag{11}$$

where σ_{eff}, the effective stress described Eq. (7), represents the solid contribution to the mechanical stress. β is the Biot's coefficient, set to 1 thanks to the hypothesis of the phases incompressibility. $p^s = S^t p^t + S^l p^l$, denoted the solid pressure, represents the fluids' contribution to the mechanical stress.

Assumption on the porous medium components and parameters motivated by literature

The stiffness of the cortex has been intensively studied (Castellano Smith et al., 2003; Kaster et al., 2011; Budday et al., 2014b, among many others). It both depends on the chosen modeling framework and the sample composition, so the values of the Young's modulus E can widely vary. In time-independent modeling, as linear elastic or hyperelastic, using linear elastic law leads to scatter values Young's modulus E, from 2.5 kPa (Wittek et al., 2009) to 8 kPa (Castellano Smith et al., 2003). Non-linear hyperelastic modeling has more homogeneous values, with E between 1.1 kPa (Kaster et al., 2011) and 3 kPa (Budday et al., 2014b). In the reproduced experimental study (Budday et al., 2015), the authors found by contact theory $E = 1.389 \pm 0.289$ kPa. Conversely, the values of Poisson's ratio ν are quite consensual in the literature, as the material is constantly described as nearly incompressible, with values varying between 0.495 (Castellano Smith et al., 2003) and 0.45 (Schiavone et al., 2009).

In Barnes et al. (2017), the extra-cellular matrix (ECM) volume fraction is estimated to be 20%. In Lei et al. (2017), the volume fraction of the interstitial fluid (IF), added to the ECM, is estimated to be between 15% and 20%. From Bender and Klose (2009), the IF fraction, strictly limited to the parenchyma, is estimated to be between 5% and 10%, and the vascular system (in Lei et al., 2017) between 3% and 5%. Finally, the distribution indicated by Azevedo et al. in Azevedo et al. (2009) for the cerebral cortex gives 20% neuron, 80% non-neuron with ±2% of uncertainty.

We define the solid scaffold as the sum of the stroma cells (membrane, epithelial and endothelial cells), the ECM, the vascular system – because blood circulation is not considered in *ex vivo* testing – and the neurons (bodies and axons). Based on the estimation provided above, we obtain the following range of values for the solid scaffold fraction: the minimum at $(0.15 - 0.1) + 0.03 + 0.18 = 0.24$ and the maximum at $0.2 + 0.1 + 0.05 + 0.22 = 0.57$. Its complement, the porosity ε, is within the range $0.43 \leq \varepsilon \leq 0.76$.

As written in Bender and Klose (2009), the IF volume fraction estimated to $0.05 \leq \varepsilon S^l \leq 0.1$. With the estimated range of porosity ε, we obtain for the liquid phase saturation: $0.065 \leq S^l \leq 0.232$; and its complement, the glial phase saturation: $0.828 \leq S^g \leq 0.935$.

As initial range of values for the liquid phase dynamic viscosity μ_l, we keep different estimation provided in Sowinski et al. (2021) for cerebral fluid, between $0.7\cdot10^{-3}$ Pa·s and $1\cdot10^{-3}$ Pa·s. For the rheology of the glial phase, as we do not have experimental data, we choose a value close to literature used for generic cells (see Sciumè et al., 2014; Santagiuliana et al., 2019) $\mu_g \approx 30$ Pa · s.

Regarding the intrinsic permeability k^s_{int} of the solid scaffold, there is still a large knowledge gap. The important difficulty to design experiment on living tissue and the preferential use of single phase solid mechanics rather than poromechanics are probably partly responsible for this problem. In 2021, Sowinski et al. (2021) reported ranges of

values for hydraulic conductivity K, using *in silico* magnetic resonance elastography. They reported hydraulic conductivity values from $2 \cdot 10^{-11}\,\mathrm{ms}^{-1}$ to $2 \cdot 10^{-10}\,\mathrm{ms}^{-1}$. Same year, Jamal et al. in Jamal et al. (2021), reported range of values for the intrinsic permeability k^s_{int}, by *ex vivo* perfusion experiment. They reported a k^s_{int} mean value of $10^{-16}\,\mathrm{m}^2$, with a strong influence of tissue anisotropy, from $2 \cdot 10^{-17}\,\mathrm{m}^2$ to $3.2 \cdot 10^{-15}\,\mathrm{m}^2$, with one order of magnitude difference if perfusion is parallel or perpendicular to the white matter fibers. Retrieve intrinsic permeability k^s_{int} from hydraulic conductivity K is not straightforward. If the ratio $\frac{k^s_{\mathrm{int}}}{\mu}$ is common to the different equivalence, the size of the sample, its density and difference of pressure could be at play. Applying the ratio on hydraulic conductivity, a dynamic viscosity μ with the order of $1 \cdot 10^{-3}\,\mathrm{Pa \cdot s}$ will lead to an intrinsic permeability k^s_{int} between $2 \cdot 10^{-14}\,\mathrm{m}^2$ and $2 \cdot 10^{-13}\,\mathrm{m}^2$, which is two orders higher than Jamal et al. (2021). In Sowinski et al. (2021), Sowinski et al. hypothesize that *in vitro* experiments tend to lead to smaller values, due to pore collapse in sampled tissue. In Jamal et al. (2021), Jamal et al. claim that these microstructural changes become significant after 6 h post-mortem, hence they perform their experiments within these 6 h. As we do not have sufficient information, we have no other choice to keep this large range, from 10^{-17} to 10^{-13}, as acceptable values of k^s_{int}.

4. Computational framework

Using the FEniCS python libraries, the solution of the problem has been done with the finite element method, with a monolithic solution process. Boundary conditions for the consolidation tests are shown in Fig. 1B and for the indentation tests in Fig. 2B. The computations have been run on a mesh of 4×20 elements for consolidation tests and 98×60 for indentation tests, both are cylindrical axis symmetric representation of the sample. The same computations have been run with meshes with three levels of refinement, with the same results.

The boundaries of the consolidation tests are shown in Fig. 1B. The fluids are free to escape to loaded boundary (drained condition) and the other boundaries are impervious. For the solid scaffold, except at the loaded boundary, its displacement is allowed only on the tangential direction (slip condition). The boundaries of the indentation tests are shown in Fig. 2B. Its boundary conditions are denoted by Γ_S the axis of symmetry, by Γ_B and Γ_C the slip boundaries prescribed in the experimental design. Γ_I is the indented surface, where the fluid is assumed under impervious condition and Γ_F the free surface.

All the codes used for computation are available on Github, at https://github.com/StephaneUrcun/BrainTissue

Local sensitivity analysis and parameters calibration

As an initial guess, we first set all the parameters within their ranges given in Section 3 paragraph '*Assumption motivated by literature*'. Seven are denoted *tissue specific*, because they are general properties, more likely to be shared by all samples: the porosity ϵ, the Poisson's ratio ν, the dynamic viscosity of the two fluid phases μ_l, μ_g, their corresponding tortuosity exponent A_l, B_g and a, the referenced pressure of the cell-ECM interplay. Young's Modulus E and intrinsic permeability k^s_{int}, which have the wider ranges, and the initial liquid phase saturation S^l_0 are denoted *sample specific* (S^l_0 varies for each sample, but within the prescribed physiological range, see Section 3 paragraph *Assumption motivated by literature*).

We perform a variance-based local sensitivity analysis on the parameters at their initial guess value ±10%, described Appendix B. We perform first order sensitivity analysis (the parameters are modified one at a time) as well as second order analysis (the 45 parameters tuples are tested to quantify parameters correlation). The parameters are strongly inter-dependent, the 45 tuples gather 87.3% of the variance, the parameters cannot be calibrated separately. The weights of the parameter tuples confirm the idea of two parameters subsets: the 21 tuples of tissue specific parameters gather 49.6%, where the 21 tuples of tissue *v.s.* sample specific parameters gather only 35.6%, see Fig. 3A, the 3 tuples of sample specific parameter are less correlated, they weigh only for 2.1%. The results of the first order are in Fig. 3B and the details of the Sobol indices can be found in Appendix B.

Table 2
Model parameters calibrated of the consolidation tests on *ex vivo* human cortex (Franceschini et al., 2006). Seven parameters, ϵ, ν, $\mu_l\,(\mathrm{Pa \cdot s})$, A_l, $\mu_g\,(\mathrm{Pa \cdot s})$, B_g and $a\,(\mathrm{Pa})$ denoted *tissue specific*, are common to all samples. Three parameters, $E\,(\mathrm{Pa})$, $k^s_{\mathrm{int}}\,(\mathrm{m}^2)$ and S^l_0, within the prescribed range $[0.065; 0.232]$, are calibrated specifically for each sample. Only one sample, 3N C2 d, is slightly below S^l_0 prescribed range.

Sample	E (Pa)	k^s_{int} (m^2)	Sl_0	RMSE
3N C2 b	4130	$2.2e^{-13}$	0.075	0.056
3N C2 d	9300	$2.1e^{-13}$	0.059	0.036
3N C2 e	3740	$4.7e^{-13}$	0.100	0.016
6N C3 a	4330	$2.9e^{-13}$	0.114	0.011
6N C3 b	3500	$6.1e^{-13}$	0.169	0.017
6N 6	7100	$2.1e^{-13}$	0.094	0.015

Shared parameters (tissue specific)	Sl_0	ϵ	ν	$\mu_l\,(\mathrm{Pa \cdot s})$	A_l	$\mu_g\,(\mathrm{Pa \cdot s})$	B_g	a
	[0.065;0.232]	0.6	0.49	$8e^{-3}$	1	35	2	800

The calibration process has been performed on all samples of the consolidation tests and on the mean curve of Test 1 of the indentation tests. It consists in a Newton algorithm on the 7 tissue specific parameters, the sample specific parameters being fixed. Once the algorithm gives no improvement (RMSE improvement below 10^{-4}), we perform, for each sample separately for the consolidation tests and for indentation Test 1, the calibration of the sample specific parameters E, k^s_{int} and S^l_0.

Measure of error

The error between numerical results y^{num} and experiments data y^{exp}, evaluated at n points, is measured in percentage by the relative root mean square error (RMSE):

$$RMSE = \sqrt{\sum_{i=1}^{n} \left(\frac{y_i^{\mathrm{exp}} - y_i^{\mathrm{num}}}{y_i^{\mathrm{exp}}} \right)^2} \tag{12}$$

5. Results

The working hypothesis of this contribution is that the time-dependent properties of cortex tissue can be modeled using a two-phase flow poroelasticity framework. This hypothesis is tested in this section to reproduce the experimental results of the consolidation tests in Franceschini et al. (2006) and the unconfined indentation tests in Budday et al. (2015). To emphasize the limit of visco-elasticity compared to poro-elasticity, a 1D confined compression test with an available analytical solution is reproduced and discussed in Appendix A.

Consolidation tests

The mechanical response of the six samples is generated using parameters shown in Table 2. All the samples share the same *tissue specific* parameters set. Fig. 4A, B shows the results of the model for the 3 Newton and 6 Newton load series respectively. We obtain accurate results for the 6 samples with an error ranged from 1.1 to 5.6%. These results are obtained by calibrating three parameters, the Young's modulus E, the intrinsic permeability k^s_{int}, and the initial saturation of liquid phase S^l_0 within the physiological range 6.5%–17.2% (with one exception sample 3N C2 d at 5.9%). All the details are referenced in Table 2.

Indentation tests

The four indentation tests have been reproduced using the same mathematical modeling (Section 3) and computational framework (Section 4) than the consolidation tests. However, these indentation tests are not specifically adapted to poromechanical modeling, so that the nature of the free surface of the sample Γ_F (see Fig. 2B) is not clearly

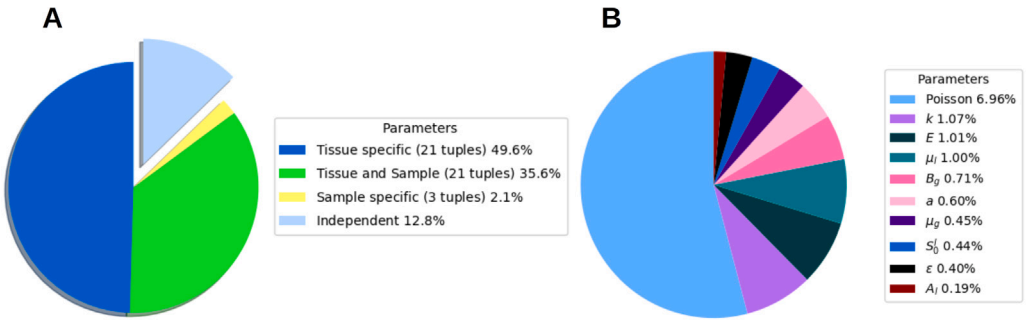

Fig. 3. Results of the second-order sensitivity analysis. **A** The parameters interaction gathers 87.1% of the solution variance, *i.e.* the parameters are strongly correlated. The 21 tuples of tissue specific parameters weight for 49.6%, the 21 tuples of tissue/sample interaction weight for 35.6%, the 3 tuples of sample specific parameter are less correlated, they weight only for 2.1%. **B** Details of the weight of parameter independent sensitivity. The Poisson's ratio ν sensitivity largely dominates the other parameters.

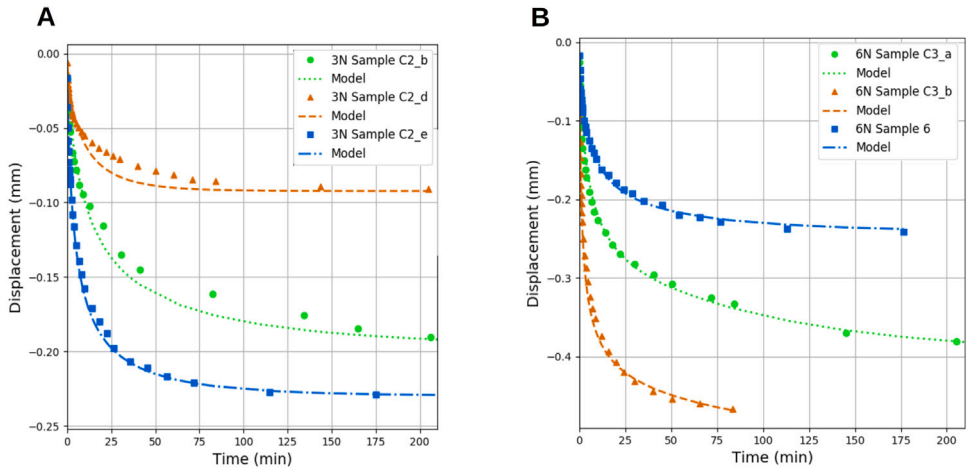

Fig. 4. Numerical reproduction of Franceschini et al. consolidation tests on *ex vivo* human cortex (Franceschini et al., 2006). Time (minutes) *vs.* Displacement (mm). **A** 3 Newton load series. Sample 3N C2 b (experimental green circle; numerical green dotted) is reproduced with 0.056 RMSE (see Eq. (12)); Sample 3N C2 d (experimental orange triangle; numerical orange dotted) with 0.036 RMSE; Sample 3N C2 e (experimental blue square; numerical blue dotted) with 0.016 RMSE. **B** 6 Newton load series. Sample 6N C3 a (experimental green circle; numerical green dotted) is reproduced with 0.011 RMSE; Sample 6N C3 b (experimental orange triangle; numerical orange dotted) with 0.017 RMSE; Sample 6N 6 (experimental blue square; numerical blue dotted) with 0.015 RMSE.

prescribed from the fluids point of view. If the cortex slice cut follows a membrane, it leads to an impervious boundary as Eq. (13a). In the case of a proper fluid drainage, this leads to a homogeneous Dirichlet condition, Eq. (13b). The intermediate case leads to a semi-pervious boundary. To our knowledge, no investigation has been done on the passive drainage of the free surface for *ex vivo* cortex tissue testing, then we adopt a convective condition, usual in mass transfer through boundaries in poromechanics (Gerard et al., 2010) Eq. (13c).

$$\frac{\partial p^\alpha}{\partial n} = 0 \quad \text{on } \Gamma_F \quad \alpha = g, l \tag{13a}$$

$$p^\alpha = 0 \quad \text{on } \Gamma_F \quad \alpha = g, l \tag{13b}$$

$$\frac{\partial p^\alpha}{\partial n} = h(p^\alpha - p_0^\alpha) \quad \text{on } \Gamma_F \quad \alpha = g, l \tag{13c}$$

Our investigation shows that a semi-pervious boundary on the sample free surface gives slightly better results than an impervious boundary for the indenter surface response evaluated in this article. With the same parameters, the influence of different boundary conditions on the free surface are shown in Fig. 5. For the sake of simplicity, we choose an impervious boundary condition on the free surface.

We identify the parameters of Budday et al. (2015) with only one test, the 1 millimeter diameter long range indentation on gray matter, denoted Test 1 in this article. Then, we validate these parameters on the other tests. The parameters of Test 1 are identified by the same process than consolidation tests, see Section 4.

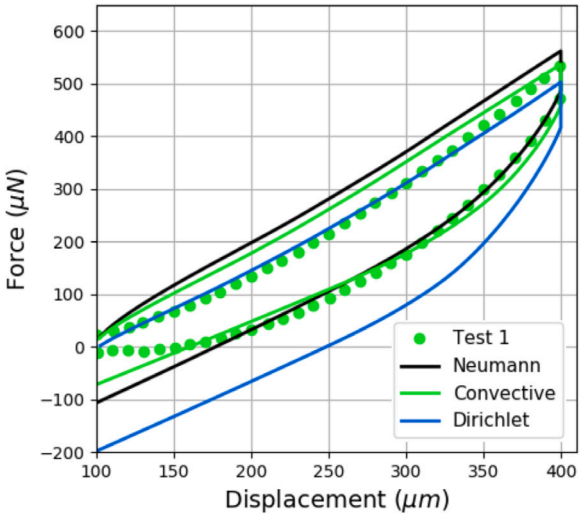

Fig. 5. Influence of the free surface boundary condition on the indenter surface response. Shared parameter set: $E = 730\,\text{Pa}$, $k^s_{\text{int}} = 3 \cdot 10^{-3}\,\text{m}^2$, $S^l_0 = 0.063$, $\varepsilon = 0.6$, $\nu = 0.49$, $\mu_l = 3 \cdot 10^{-3}\,\text{Pa}\cdot\text{s}$, $A_l = 1$, $\mu_g = 30\,\text{Pa}\cdot\text{s}$ and $B_g = 2$. Experimental (gree dotted); Neumann (black) impervious condition Eq. (13a); Dirichlet (blue) drained condition Eq. (13b); Convective (green), with the additional parameter $h = 10^{-4}$, Eq. (13c) semi-pervious condition.

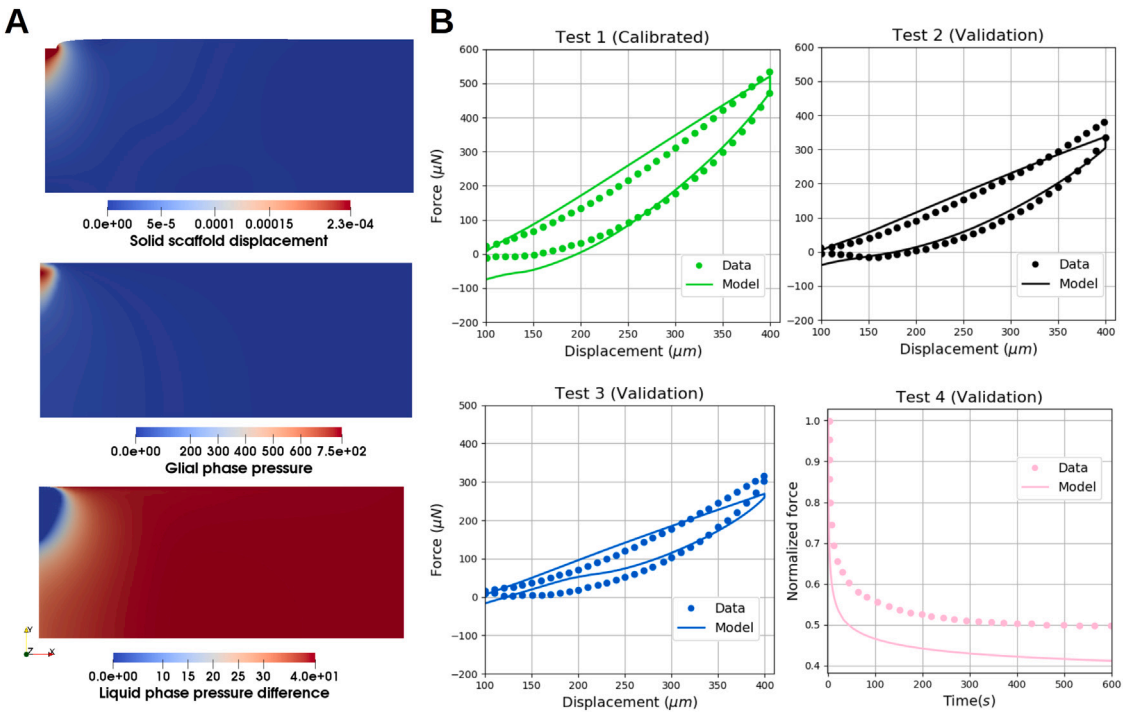

Fig. 6. Indentation tests on *ex vivo* bovine cortex (Budday et al., 2015): validation of the calibrated parameters on Test 1. **A** Example of the simulation results on Test 1. At 230 μm indentation depth, the glial pressure raised to 780 Pa and flush out the liquid phase (*i.e.* 0 Pa of pressure difference p^{lg} in this area). Note that the liquid phase is subjected to a pressure p^{l} of a few hundreds of Pascal at the indenter zone and only 40 Pa at the sample boundaries. **B** Test 1, experimental (green dotted), numerical (green plain line), RMSE = 12.7%; Test 2, experimental (black dotted), numerical (black plain line), RMSE = 13.5%; Test 3, experimental (blue dotted), numerical (blue plain line), RMSE = 16.7%; Test 4, experimental (pink dotted), numerical (pink plain line), RMSE = 18.3%.

Table 3
Parameters for indentation tests on *ex vivo* bovin cortex. Validation (V) on Test 2, 3 and 4 of the calibrated (C) parameters of the Test 1. Specific calibration (C) of the Test 4. Seven parameters, ϵ, ν, μ_l (Pa · s), A_l, μ_g (Pa · s), B_g and a (Pa) denoted *tissue specific*, are common to all samples.

Sample	E (Pa)	k^s_{int} (m^2)	Sl_0	RMSE
Test 1 (C)	605	$2.8e^{-12}$	0.027	0.127
Test 2 (V)	605	$2.8e^{-12}$	0.027	0.135
Test 3 (V)	605	$2.8e^{-12}$	0.027	0.167
Test 4 (V)	605	$2.8e^{-12}$	0.027	0.183
Test 4 (C)	1100	$4.2e^{-12}$	0.047	0.099

Shared parameters (tissue specific)	Sl_0	ϵ	ν	μ_l (Pa · s)	A_l	μ_g (Pa · s)	B_g	a
	[0.065;0.232]	0.5	0.47	3^{-3}	1	30	1	400

The resulting parameters of Test 1 (12.7% RMSE) are validated on Test 2, 3 and 4, see Fig. 6. It shows that the calibrated parameters lose accuracy but remain capable of reproducing the different tests. The change in the indenter diameter Test 2 slightly increases the error (13.5% RMSE). The results degradation is more significant when loading rates change in Test 3 (16.7% RMSE) or for the relaxation Test 4 (18.3% RMSE). Test 4 has been calibrated independently (10.3% RMSE), see Fig. 7, giving a different profile with E almost twice higher, see Table 3. The calibrated parameters of Test 1 give a value of S^l_0 below the prescribed physiological range (< 6.5%), whereas the calibrated S^l_0 of Test 4 is closer to the physiological range (see Table 3).

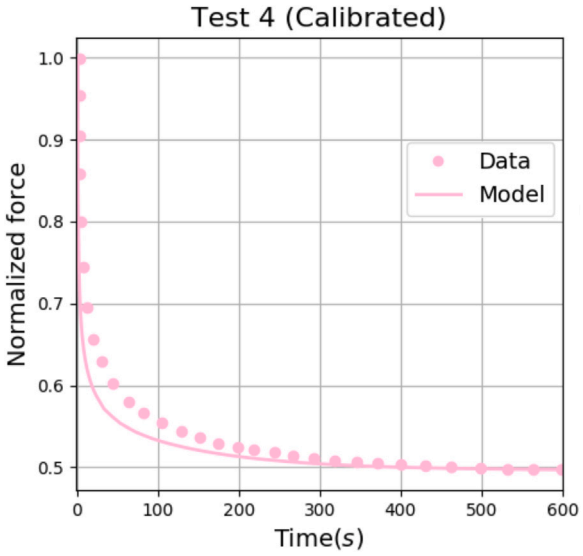

Fig. 7. Indentation tests on *ex vivo* bovine cortex (Budday et al., 2015): calibration of the parameters of Test 4. Experimental (pink dotted), numerical (pink plain line), RMSE = 10.3%.

6. Discussion

The strong time-dependent mechanical behavior of the cortex is generally attributed to both the intrinsic viscoelasticity of the solid phase and fluid flow-induced poroelasticity but the relative contributions of the two are unclear. Conventional approaches combine viscoelastic and poroelastic behaviors into a single framework to be able to reproduce experimental data (Franceschini et al., 2006; Hosseini-Farid et al., 2020).

In this contribution we propose to implement a two-phase flow poroelastic model of the cortex to capture the consolidation, the relaxation and the sensitivity of a set of selected load rates and investigate the dissipation mechanisms. Two sets of experiments are reproduced: the consolidation test of Franceschini et al. (2006) and the unconfined indentation test of Budday et al. (2015). Our results show that the

experimental curves can be reproduced without the need to resort to viscous effects, by adding an additional fluid phase.

First, we note that we examine in this paper two mechanical tests which are considerably different. For the consolidation test a load as high as 6 Newton is applied on the delicate structure of the cortex, which corresponds to a pressure of 8440 Pa. In the indentation test, the load is approximately 0.6 mN (that is 4 orders of magnitude smaller), corresponding to a 20 Pa pressure. The two tests are therefore very dissimilar in the way the sample is loaded, deformed and, possibly, damaged.

We estimate material parameters associated with the models we develop. We then compare those parameters with those published in the literature. We consider those parameters through the lens of the PhD thesis of Morin et al. (2017, Chapter 6). Within this scope, we focus on rheological parameters extracted from confined/unconfined experiments on human/animal gray matter.

The stiffness values (Young's modulus) reported in the literature, computed by considering gray matter as a monolithic solid, are widely scattered (1.1 to 8 kPa). In the unconfined indentation case, these stiffness values are much higher than those we obtain (0.6–1.2 kPa). This observation is explained by the fact that the stiffness we "measure" consists in both a solid component and a fluid component, thereby decreasing the effective stiffness contribution of the solid phase Young's modulus. The values we obtain for E in the confined consolidation tests are six times as high as those obtained in the unconfined indentation case ($E = 5.35 \pm 2.12$ kPa). This could seem surprising. The possibility of different stiffness between human and animal – simian, bovine and porcine – brain have led to contradictory results (see Prange and Margulies, 2002; Nicolle et al., 2004). We looked for a possible explanation for this stiffness discrepancy within environmental conditions such as: sample preservation, hydration and temperature. The loss of hydration and temperature have cumulative effects. All other conditions remaining equal, temperatures of 24 °C and 37 °C will lead to a stiffness 40% lower, but the same variation with dehydration will lead to a stiffness 5 fold higher (see Forte et al., 2017 for a detailed study on this topic). However, according to the ranges given in Forte et al. (2017), the confined consolidation and unconfined indentation tests were made in sufficiently close environmental conditions to rule out this hypothesis.

We therefore hypothesize that, during confined consolidation, pore locking may take place, leading to the creation of fluid "pockets" within the structure. This incomplete consolidation results in an effective stiffening of the sample and thereby in an increase of the apparent Young's modulus.

Regarding the Poisson's values, they correspond to the literature consensus with $\nu = 0.47$ in the unconfined case, and $\nu = 0.49$ in the confined case.

In the confined case, we obtain one order of magnitude smaller permeabilities than in the unconfined case. The intrinsic permeabilities we evaluate, amended by their respective relative permeabilities, are however within the experimental range provided in the literature. Such decrease in permeability can be caused by the pore locking phenomenon described above. Moreover, the consolidation tests were performed within 12 h, as opposed to 6 h for the indentation tests. This time delay could lead to significant changes in the microstructure (Jamal et al., 2021), which also alters the permeability.

The review of Budday et al. (2019) pointed out the promising coupling of poro-viscoelasticity, as it takes account of both the interplay between interstitial fluid and stroma and the time-dependent response of cellular phase. The model proposed by Franceschini et al. in Franceschini et al. (2006) along with their experiments is an example of this coupling. We show in this article that a one-phase flow coupled with a viscoelastic solid, in the reproduced loading scenarii, can be replaced by a two-phase flow with an elastic solid. The two different dynamic viscosities ($\mu_l = 5.5 \pm 2.5\, 10^{-3}$ Pa·s and $\mu_c = 32.5 \pm 2.5$ Pa·s) give two different characteristic times. They are comparable to the two-terms Prony series proposed in the viscoelastic parameter identification of human brain tissue of Budday et al. in Budday et al. (2017) characterized by $\tau_1 = 0.18$ s and $\tau_1 = 63.5$ s. Moreover, our parameters are not dependent on the geometry, as shown in the Appendix A. The fact that the tissue characteristics are build upon experimental findings offers a reliable way for a tissue specific pre-calibration. The sample calibration is only done on three parameters, which is equivalent, in computational cost, to the classic hyperelastic models (Yeoh, 1993; Ogden and Hill, 1972).

Even if we endeavour to build our model on experimental matter, we are aware of its limits. A solid scaffold described as the sum of the stroma, the vascular network and the ECM is obviously non-linear. We have not included dependency between permeability and porosity in our model (the interested reader could find a presentation in Meroi and Schrefler, 1995), whereas in confined deformation with an incompressibility hypothesis, the main part of the deformation is absorbed by the pores. Adding this relation would lead to closer values of intrinsic permeability k^s_{int} between indentation and consolidation, and partially suppress the artificial stiffness of consolidation parameters, by increasing the fluids supported stress. We can also point out that the total stress relationship we used, along with a Biot coefficient equal to 1 is a strong hypothesis. The incompressibility of the fluids is not to be questioned. Yet, micro-structural changes due to post-mortem experiments or mechanical damage may increase solid scaffold compressibility. Only three load rates are reproduced in this paper (1 μm/s, 5 μm/s and 100 μm/s), a large panel still remains to explore. Likewise, our model response on various loading scenarii – tension or shear – or experimental condition – such as temperature dependency – remains open. As a consequence, our results are only relevant at room temperature under humidity control.

The results in this paper indicate that multi-phase models could be a strong basis for the description of biological tissue such as the brain, *ex vivo* and *in vivo*, as some advanced models can reproduced interplay of vessels and tissue (Sciumè, 2021; Ehlers and Wagner, 2015b). We hope this contribution will encourage the community to develop new experimental techniques which are compatible with poro-mechanical models. More specifically, the enforcement of boundary conditions on free surfaces could help the modeling of different drainage conditions.

Beyond experimental setups, another open challenge lies in the ability of models to be transferred from one observational/experimental situation to another. For this work to have impact in a clinical setting, methods must be developed to transfer parameters and models from one set of patients to another. We believe that a quantitative approach to this would be to develop robust model selection approaches from experimental or clinical data (Zeraatpisheh et al., 2021).

CRediT authorship contribution statement

Stéphane Urcun: Conceptualization (developed the mathematical model), Methodology (contributed on design of sensitive analysis), Software (implemented the model in the finite element code and performed numerical simulations), Validation (developed of a cross-validation, methodology), Investigation (conducted a research on experimental design to reproduce), Writing – original draft, (wrote the initial draft), Writing – review & editing, Visualization (contributed to the data visualization). **Pierre-Yves Rohan:** Investigation (conducted a research on experimental design to reproduce), Writing – original draft (wrote the initial draft), Writing – review & editing. **Giuseppe Sciumè:** Conceptualization (developed the mathematical model), Writing – review & editing, Visualization (contributed to the data visualization). **Stéphane P.A. Bordas:** Methodology (contributed on design of sensitive analysis), Validation (developped of a cross-validation, methodology), Writing – review & editing, Supervision.

Declaration of competing interest

The authors declare that they have no known competing financial interests or personal relationships that could have appeared to influence the work reported in this paper.

Table B.4
Sobol indices of the first-order local sensitivity analysis.

Parameter	θ	$S_i(\%)$
E	0.0426	8.29
ν	0.2384	56.7
k^s_{int}	−0.0430	8.74
ϵ	−0.0304	3.32
μ_l	0.0346	8.17
μ_g	0.0114	3.70
A_l	0.0002	1.58
B_g	0.0208	5.80
S^l_0	−0.0256	3.63

Acknowledgments

The results presented in this paper were carried out using the HPC facilities of the University of Luxembourg (Varrette et al., 2014) (see https://hpc.uni.lu).

Appendix A. Viscoelastic modeling limitation on consolidation test reproduction

Let us consider two reference models: a one solid-one fluid poroelastic model and a rheological viscoelastic model constituted by a Kelvin–Voigt chain; and use these two models to simulate a 1D confined compression test. In this test the tissue is constrained in a cylindrical chamber and compressed at the top surface with a constant pressure P_0. The specimen is fully sealed with the exception of the top and the bottom surface where a porous membrane allows drainage of the inside fluid during the test. The geometry and boundary conditions of the test are represented in Fig. 4A. The simplicity of the two considered models jointed with the simplicity of the considered test allows to derive the analytical solution for both modeling approaches (see Verruijt, 2013 for the poromechanical model). For the one-fluid one-solid poroelastic model:

$$p_z(z,t) = P_0 \frac{4}{\pi} \sum_{k=1}^{\infty} \frac{(-1)^{k-1}}{2k-1} \cos\left((2k-1)\frac{\pi}{2}\frac{z}{L}\right) \exp\left((2k-1)^2 \frac{\pi^2}{4}\frac{c_v t}{h^2}\right) \tag{A.1}$$

with the consolidation coefficient under the hypothesis of phases incompressibility:

$$c_v = \frac{kM}{\mu} \tag{A.2}$$

with M the longitudinal modulus:

$$M = \frac{E(1-\nu)}{(1+\nu)(1-2\nu)} \tag{A.3}$$

E the Young's modulus and ν the Poisson's ratio.

For the viscoelastic Kelvin–Voigt chain:

$$u_z(z,t) = \frac{P_0 z}{M}\left[1 - \exp\left(-\frac{Et}{\eta}\right)\right] \tag{A.4}$$

We see that the poroelastic model is governed by the parameters E, ν and the ratio $\frac{k}{\mu}$ and the viscoelastic model by E, ν and η. However, the analytical solution of the porous model contains h, the sample height, which strongly influence the consolidation time. Then, once the parameters of the porous model are calibrated, they will remain relevant when the height of the sample varies.

Appendix B. Variance-based local sensitivity analysis

We performed a variance-based local sensitivity study of the finite element solution on the parameters as follows:

- A first-order analysis, the 9 parameters are disturbed one at a time respectively of ±10%.
- Interaction analysis, the 36 parameters tuples are evaluated simultaneously disturbed.

All the results were interpreted with a polynomial model in order to quantify their weights in the solution variance, referred to as Sobol indices. The initial guess of the parameters set was: $E = 3500\,\text{Pa}$, $\nu = 0.45$, $k = 10^{-13}\,\text{m}^2$, $\epsilon = 0.55$, $\mu_l = 8 \cdot 10^{-3}\,\text{Pa}\cdot\text{s}$, $\mu_g = 35\,\text{Pa}\cdot\text{s}$, $A_l = 1$, $B_g = 2$ and $S^l_0 = 0.012$. It gives the base error J_0.

First-order analysis

Each parameter is disturbed one at a time respectively of ±10%, giving the corresponding error $\tilde{J}$. The relative variations of the error were calculated as follows:

$$\text{Var} = \frac{\tilde{J} - J_0}{J_0} \tag{B.1}$$

where J_0 is the error with the parameters at their initial values. In order to quantify the impact of each parameter, the following linear model was set:

$$\text{Var} = 1 + \sum_i \theta_i \alpha_i \tag{B.2}$$

Table B.5
Sobol indices of the second-order local sensitivity analysis.

Parameters correlation						Parameters independence	
Tissue specific 49.5%	S_{ij} (%)	Tissue/Sample 35.4%	S_{ij} (%)	Sample specific 2.1%	S_{ij} (%)	12.8%	S_i (%)
(ν, ϵ)	5.34	(E, ν)	8.07	(E, k)	0.45	E	1.01
(ν, μ_l)	7.59	(E, ϵ)	0,31	(E, S^l_0)	0.26	ν	6.96
(ν, μ_g)	6.59	(E, μ_l)	1.83	(k^s_{int}, S^l_0)	1.36	k^s_{int}	1.07
(ν, A_l)	6.19	(E, μ_g)	1,22			ϵ	0.40
(ν, B_g)	7.14	(E, A_l)	0.90			μ_l	1.00
(ν, a)	7.06	(E, a)	1.40			a	0.60
(ϵ, μ_l)	0.31	(E, B_g)	1.44			μ_g	0.45
(ϵ, μ_g)	0.33	(k^s_{int}, ν)	4.13			A_l	0.19
(ϵ, A_l)	0.37	(k^s_{int}, ϵ)	1.87			B_g	0.71
(ϵ, B_g)	0.37	(k^s_{int}, μ_l)	0.44			S^l_0	0.44
(ϵ, a)	0.43	(k^s_{int}, a)	0.72				
(μ_l, μ_g)	1.16	(k^s_{int}, μ_g)	1.01				
(μ_l, A_l)	0.88	(k^s_{int}, A_l)	1.28				
(μ_l, B_g)	1.38	(k^s_{int}, B_g)	0.77				
(μ_l, a)	1.37	(S^l_0, ν)	5.15				
(μ_g, A_l)	0.30	(S^l_0, ϵ)	0.28				
(μ_g, B_g)	0.81	(S^l_0, μ_l)	0.25				
(μ_g, a)	0.77	(S^l_0, a)	3.23				
(A_l, B_g)	1.14	(S^l_0, μ_g)	0.32				
(A_l, a)	0.49	(S^l_0, A_l)	0.61				
(B_g, a)	1.40	(S^l_0, B_g)	1.29				

where α_i is an auxiliary parameter $\in [-1, +1]$ representing the perturbations of $\pm 10\%$ of the ith parameter and θ_i the slope of the variation.

In a first-order analysis, the influence of the ith parameter is given by the Sobol indices:

$$S_i = \frac{\theta_i^2}{\sum_i \theta_i^2} \tag{B.3}$$

The results of the first-order analysis are reported in Table B.4.

Interaction analysis

We evaluate the correlation between parameters. The 36 tuples $(\alpha_i, \alpha_j)_{i>j}$ have been evaluated at $\pm 10\%$. The corresponding polynomial model becomes:

$$\mathrm{Var} = 1 + \sum_i \theta_i \alpha_i + \sum_{ij, i>j} \theta_{ij} \alpha_i \alpha_j \tag{B.4}$$

with the respective Sobol indices:

$$S_i = \frac{\theta_i^2}{\sum_i \theta_i^2 + \sum_{ij,i>j} \theta_{ij}^2} \quad \text{and} \quad S_{ij} = \frac{\theta_{ij}^2}{\sum_i \theta_i^2 + \sum_{ij,i>j} \theta_{ij}^2} \tag{B.5}$$

The results are reported in Table B.5.

References

Azevedo, Frederico A.C., Carvalho, Ludmila R.B., Grinberg, Lea T., Farfel, José Marcelo, Ferretti, Renata E.L., Leite, Renata E.P., Filho, Wilson Jacob, Lent, Roberto, Herculano-Houzel, Suzana, 2009. Equal numbers of neuronal and nonneuronal cells make the human brain an isometrically scaled-up primate brain. J. Comp. Neurol. 513 (5), 532–541.

Barnes, Matthew J., Przybyla, Laralynne, Weaver, Valerie M., Ewald, Andrew, 2017. Tissue mechanics regulate brain development, homeostasis and disease. J. Cell Sci. 130 (1), 71–82.

Basilio, Andrew V., Xu, Peng, Takahashi, Yukou, Yanaoka, Toshiyuki, Sugaya, Hisaki, Ateshian, Gerard A., Morrison III, Barclay, 2019. Simulating cerebral edema and delayed fatality after traumatic brain injury using triphasic swelling biomechanics. Traffic Inj. Prev. 20 (8), 820–825. http://dx.doi.org/10.1080/15389588.2019.1663347.

Bender, Benjamin, Klose, Uwe, 2009. Cerebrospinal fluid and interstitial fluid volume measurements in the human brain at 3T with EPI. Magn. Reson. Med. 61 (4), 834–841.

Biot, Maurice A., 1941. General theory of three-dimensional consolidation. J. Appl. Phys. 12 (2), 155–164.

Budday, Silvia, Nay, Richard, de Rooij, Rijk, Steinmann, Paul, Wyrobek, Thomas, Ovaert, Timothy C., Kuhl, Ellen, 2015. Mechanical properties of gray and white matter brain tissue by indentation. J. Mech. Behav. Biomed. Mater. 46, 318–330.

Budday, Silvia, Ovaert, Timothy C., Holzapfel, Gerhard A., Steinmann, Paul, Kuhl, Ellen, 2019. Fifty shades of brain: A review on the mechanical testing and modeling of brain tissue. Arch. Comput. Methods Eng. 14, 931–965.

Budday, Silvia, Raybaud, Charles, Kuhl, Ellen, 2014a. A mechanical model predicts morphological abnormalities in the developing human brain. Sci. Rep. 4 (1), 5644.

Budday, Silvia, Raybaud, Charles, Kuhl, Ellen, 2014b. A mechanical model predicts morphological abnormalities in the developing human brain. Sci. Rep. 4, 266–273.

Budday, S., Sommer, G., Holzapfel, G.A., Steinmann, P., Kuhl, E., 2017. Viscoelastic parameter identification of human brain tissue. J. Mech. Behav. Biomed. Mater. 74, 463–476.

Budday, S., Sommer, G., Paulsen, F., Holzapfel, G.A., Steinmann, P., Kuhl, E., 2018. Region- and loading-specific finite viscoelasticity of human brain tissue. PAMM 18 (1), e201800169.

Bui, Huu Phuoc, Tomar, Satyendra, Courtecuisse, Hadrien, Audette, Michel, Cotin, Stéphane, Bordas, Stéphane P.A., 2018a. Controlling the error on target motion through real-time mesh adaptation: Applications to deep brain stimulation. Int. J. Numer. Methods Biomed. Eng. 34 (5), e2958, e2958 cnm.2958.

Bui, Huu Phuoc, Tomar, Satyendra, Courtecuisse, Hadrien, Cotin, Stéphane., Bordas, Stéphane P.A., 2018b. Real-time error control for surgical simulation. IEEE Trans. Biomed. Eng. 65 (3), 596–607.

Castellano Smith, Andrew D., Crum, William R., Hill, Derek L.G., Thacker, Neil A., Bromiley, Paul A., 2003. Biomechanical simulation of atrophy in MR images. In: Milan, Sonka, Fitzpatrick, J. Michael (Eds.), In: Medical Imaging 2003: Image Processing, vol. 5032, International Society for Optics and Photonics, SPIE, pp. 481–490.

Chatelin, S., Constantinesco, André, Willinger, Rémy, 2010. Fifty years of brain tissue mechanical testing: From in vitro to in vivo investigations. Biorheology 47 (5–6), 255–276.

Cheng, Shaokoon, Bilston, Lynne E., 2007. Unconfined compression of white matter. J. Biomech. 40 (1), 117–124.

Comellas, Ester, Budday, Silvia, Pelteret, Jean-Paul, Holzapfel, Gerhard A., Steinmann, Paul, 2020. Modeling the porous and viscous responses of human brain tissue behavior. Comput. Methods Appl. Mech. Engrg. 369, 113128.

Dutta-Roy, Tonmoy, Wittek, Adam, Miller, Karol, 2008. Biomechanical modelling of normal pressure hydrocephalus. J. Biomech. 41 (10), 2263–2271.

Ehlers, Wolfgang, Wagner, Arndt, 2015a. Multi-component modelling of human brain tissue: A contribution to the constitutive and computational description of deformation, flow and diffusion processes with application to the invasive drug-delivery problem. Comput. Methods Biomech. Biomed. Eng. 18 (8), 861–879, PMID: 24261340.

Ehlers, Wolfgang, Wagner, Arndt, 2015b. Multi-component modelling of human brain tissue: A contribution to the constitutive and computational description of deformation, flow and diffusion processes with application to the invasive drug-delivery problem. Comput. Methods Biomech. Biomed. Eng. 18 (8), 861–879, PMID: 24261340.

Fletcher, Tim L., Kolias, Angelos G., Hutchinson, Peter J.A., Sutcliffe, Michael P.F., 2014. Development of a finite element model of decompressive craniectomy. PLoS One 9 (7), 1–9.

Forero Rueda, M.A., Cui, L., Gilchrist, M.D., 2011. Finite element modelling of equestrian helmet impacts exposes the need to address rotational kinematics in future helmet designs. Comput. Methods Biomech. Biomed. Eng. 14 (12), 1021–1031. http://dx.doi.org/10.1080/10255842.2010.504922.

Forte, Antonio E., Gentleman, Stephen M., Dini, Daniele, 2017. On the characterization of the heterogeneous mechanical response of human brain tissue. Biomech. Model. Mechanobiol. 16, 907–920.

Franceschini, G., Bigoni, D., Regitnig, P., Holzapfel, G.A., 2006. Brain tissue deforms similarly to filled elastomers and follows consolidation theory. J. Mech. Phys. Solids 54 (12), 2592–2620.

van Genuchten, M.Th., 1980. A closed-form equation for predicting the hydraulic conductivity of unsaturated soils. Soil Sci. Am. J. 44 (5), 892–898.

Gerard, Pierre, Léonard, Angélique, Masekanya, Jean-Pierre, Charlier, Robert, Collin, Frédéric, 2010. Study of the soil–atmosphere moisture exchanges through convective drying tests in non-isothermal conditions. Int. J. Numer. Anal. Methods Geomech. 34 (12), 1297–1320.

Gray, William G., Miller, Cass T., 2014. Introduction to the Thermodynamically Constrained Averaging Theory for Porous Medium Systems. Springer.

Hakim, S, Venegas, JG, Burton, JD, 1976. The physics of the cranial cavity, hydrocephalus and normal pressure hydrocephalus: mechanical interpretation and mathematical model. Surgical Neurol. (ISSN: 0090-3019) 5 (3), 187âĂŤ210.

Haslach, Henry W., Leahy, Lauren N., Riley, Peter, Gullapalli, Rao, Xu, Su, Hsieh, Adam H., 2014. Solid–extracellular fluid interaction and damage in the mechanical response of rat brain tissue under confined compression. J. Mech. Behav. Biomed. Mater. 29, 138–150.

Hosseini-Farid, Mohammad, Ramzanpour, Mohammadreza, McLean, Jayse, Ziejewski, Mariusz, Karami, Ghodrat, 2020. A poro-hyper-viscoelastic rate-dependent constitutive modeling for the analysis of brain tissues. J. Mech. Behav. Biomed. Mater. 102, 103475.

Jamal, Asad, Mongelli, Maria Teresa, Vidotto, Marco, Madekurozwa, Michael, Bernardini, Andrea, Overby, Darryl R., De Momi, Elena, y Baena, Ferdinando Rodriguez, Sherwood, Joseph M., Dini, Daniele, 2021. Infusion mechanisms in brain white matter and their dependence on microstructure: An experimental study of hydraulic permeability. IEEE Trans. Biomed. Eng. 68 (4), 1229–1237.

Kaster, T., Sack, I., Samani, A., 2011. Measurement of the hyperelastic properties of ex vivo brain tissue slices. J. Biomech. 44 (6), 1158–1163.

Lang, Georgina E., Stewart, Peter S., Vella, Dominic, Waters, Sarah L., Goriely, Alain, 2014. Is the donnan effect sufficient to explain swelling in brain tissue slices? J. R. Soc. Interface 11 (96), 20140123.

Lefever, Joel A., García, José Jaime, Smith, Joshua H., 2013. A patient-specific, finite element model for noncommunicating hydrocephalus capable of large deformation. J. Biomech. 46 (8), 1447–1453.

Lei, Yiming, Han, Hongbin, Yuan, Fan, Javeed, Aqeel, Zhao, Yong, 2017. The brain interstitial system: Anatomy, modeling, in vivo measurement, and applications. Prog. Neurobiol. 157, 230–246, New Perspectives on Healthy Aging.

Li, Xiaogai, von Holst, Hans, Kleiven, Svein, 2013. Influences of brain tissue poroelastic constants on intracranial pressure (ICP) during constant-rate infusion. Comput. Methods Biomech. Biomed. Eng. 16 (12), 1330–1343, PMID: 22452461.

MacManus, David B., Pierrat, Baptiste, Murphy, Jeremiah G., Gilchrist, Michael D., 2017. A viscoelastic analysis of the p56 mouse brain under large-deformation dynamic indentation. Acta Biomater. 48, 309–318.

Mascheroni, Pietro, Stigliano, Cinzia, Carfagna, Melania, Boso, Daniela P., Preziosi, Luigi, Decuzzi, Paolo, Schrefler, Bernhard A., 2016. Predicting the growth of glioblastoma multiforme spheroids using a multiphase porous media model. Biomech. Model. Mechanobiol. 15 (1), 1215–1228.

Meroi, E.A., Schrefler, B.A., 1995. Large Strain Static and Dynamic Hydro-Mechanical Analysis of Porous Media. Springer Vienna, Vienna, pp. 397–447.

Morin, Fanny, Chabanas, Matthieu, Courtecuisse, Hadrien, Payan, Yohan, 2017. Biomechanical Modeling of Brain Soft Tissues for Medical Applications. Academic Press.

Nagashima, Tatsuya, Tamaki, Norihiko, Matsumoto, Satoshi, Horwitz, Barry, Seguchi, Yasuyuki, 1987. Biomechanics of hydrocephalus: A new theoretical model. Neurosurgery 21 (6), 898–904.

Nicolle, S., Lounis, M., Willinger, R., 2004. Shear properties of brain tissue over a frequency range relevant for automotive impact situations: New experimental results. Stapp Car Crash J. 11, 239–258.

Ning, Xinguo, Zhu, Qiliang, Lanir, Yoram, Margulies, Susan S., 2006. A transversely isotropic viscoelastic constitutive equation for brainstem undergoing finite deformation. J. Biomech. Eng. 128 (6), 925–933.

Ogden, Raymond William, Hill, Rodney, 1972. Large deformation isotropic elasticity – on the correlation of theory and experiment for incompressible rubberlike solids. Proc. R. Soc. Lond. Ser. A Math. Phys. Eng. Sci. 326 (1567), 565–584.

Owler, Brian K., Pena, Alonso, Momjian, Shahan, Czosnyka, Zofia, Czosnyka, Marek, Harris, Neil G., Smielewski, Piotr, Fryer, Tim, Donvan, Tim, Carpenter, Adrian, Pickard, John D., 2004. Changes in cerebral blood flow during cerebrospinal fluid pressure manipulation in patients with normal pressure hydrocephalus: A methodological study. J. Cereb. Blood Flow Metab. 24 (5), 579–587, PMID: 15129190.

Prange, Michael T., Margulies, Susan S., 2002. Regional, directional, and age-dependent properties of the brain undergoing large deformation. J. Biomech. Eng. 124 (2), 244–252.

Rashid, Badar, Destrade, Michel, Gilchrist, Michael D., 2012. Mechanical characterization of brain tissue in compression at dynamic strain rates. J. Mech. Behav. Biomed. Mater. 10, 23–38.

Santagiuliana, Raffaella, Milosevic, Miljan, Milicevic, Bogdan, Sciumè, Giuseppe, Simic, Vladimir, Ziemys, Arturas, Kojic, Milos, Schrefler, Bernhard A., 2019. Coupling tumor growth and bio distribution models. Biomed. Microdevices 21.

Schiavone, P., Chassat, F., Boudou, T., Promayon, E., Valdivia, F., Payan, Y., 2009. In vivo measurement of human brain elasticity using a light aspiration device. Med. Image Anal. 13 (4), 673–678.

Sciumè, Giuseppe, 2021. Mechanistic modeling of vascular tumor growth: An extension of Biot's theory to hierarchical bi-compartment porous medium systems. Acta Mech. 232, 1445–1478.

Sciumè, G., Boso, D.P., Gray, W.G., Cobelli, C., Schrefler, B.A., 2014a. A two-phase model of plantar tissue: A step toward prediction of diabetic foot ulceration. Int. J. Numer. Methods Biomed. Eng. 30 (11), 1153–1169.

Sciumè, Giuseppe, Ferrari, Mauro, Schrefler, Bernhard A., 2014b. Saturation–pressure relationships for two- and three-phase flow analogies for soft matter. Mech. Res. Commun. 62, 132–137.

Sciumè, G., Santagiuliana, R., Ferrari, M., Decuzzi, P., Schrefler, B.A., 2014. A tumor growth model with deformable ECM. Phys. Biol. 11 (6).

Seo, Hyeon, Kim, Donghyeon, Jun, Sung Chan, 2016. Effect of anatomically realistic full-head model on activation of cortical neurons in subdural cortical stimulation-A computational study. Sci. Rep. 6, 27353.

Sobey, Ian, Eisentraeger, Almut, Wirth, B., Czosnyka, Marek, 2012. Simulation of cerebral infusion tests using a poroelastic model. Int. J. Numer. Anal. Model. Ser. B 3 (01), 52–64.

Sowinski, Damian R., McGarry, Matthew D.J., Van Houten, Elijah E.W., Gordon-Wylie, Scott, Weaver, John B., Paulsen, Keith D., 2021. Poroelasticity as a model of soft tissue structure: Hydraulic permeability reconstruction for magnetic resonance elastography in silico. Front. Phys. 8, 637.

Varrette, S., Bouvry, P., Cartiaux, H., Georgatos, F., 2014. Management of an academic HPC cluster: The UL experience. In: Proc. of the 2014 Intl. Conf. on High Performance Computing & Simulation. HPCS 2014, Bologna, Italy, IEEE, pp. 959–967.

Verruijt, A., 2013. Theory and Problems of Poroelasticity.

Wittek, Adam, Hawkins, Trent, Miller, Karol, 2009. On the unimportance of constitutive models in computing brain deformation for image-guided surgery. Biomech. Model. Mechanobiol. 8, 77–84.

Yeoh, O., 1993. Some forms of the strain energy function for rubber. Rubber Chem. Technol. 66, 754–771.

Zeraatpisheh, Milad, Bordas, Stephane P.A., Beex, Lars A.A., 2021. Bayesian model uncertainty quantification for hyperelastic soft tissue models. Data-Cent. Eng. 2, e9.